

# Subsurface damage pattern and formation mechanism of monocrystalline $\beta$ - $\text{Ga}_2\text{O}_3$ in grinding process

Xin YANG, Renke KANG, Shang GAO (✉), Zihe WU, Xianglong ZHU

Key Laboratory for Precision and Non-Traditional Machining Technology of Ministry of Education, Dalian University of Technology, Dalian 116024, China

✉ Corresponding author. E-mail: gaoshang@dlut.edu.cn (Shang GAO)

© Higher Education Press 2022

**ABSTRACT** Monocrystalline beta-phase gallium oxide ( $\beta$ - $\text{Ga}_2\text{O}_3$ ) is a promising ultrawide bandgap semiconductor material. However, the deformation mechanism in ultraprecision machining has not yet been revealed. The aim of this study is to investigate the damage pattern and formation mechanism of monocrystalline  $\beta$ - $\text{Ga}_2\text{O}_3$  in different grinding processes. Transmission electron microscopy was used to observe the subsurface damage in rough, fine, and ultrafine grinding processes. Nanocrystals and stacking faults existed in all three processes, dislocations and twins were observed in the rough and fine grinding processes, cracks were also observed in the rough grinding process, and amorphous phase were only present in the ultrafine grinding process. The subsurface damage thickness of the samples decreased with the reduction in the grit radius and the grit depth of cut. Subsurface damage models for grinding process were established on the basis of the grinding principle, revealing the mechanism of the mechanical effect of grits on the damage pattern. The formation of nanocrystals and amorphous phase was related to the grinding conditions and material characteristics. It is important to investigate the ultraprecision grinding process of monocrystalline  $\beta$ - $\text{Ga}_2\text{O}_3$ . The results in this work are supposed to provide guidance for the damage control of monocrystalline  $\beta$ - $\text{Ga}_2\text{O}_3$  grinding process.

**KEYWORDS** monocrystalline beta-phase gallium oxide, grinding process, subsurface damage, nanocrystals, amorphous phase

## 1 Introduction

Gallium oxide ( $\text{Ga}_2\text{O}_3$ ) has received widespread attention in recent years due to its ultrawide bandgap (4.8 eV) and photovoltaic properties [1–3]. Its Baliga figure of merit (3200) is significantly higher than that of third-generation semiconductor materials, such as GaN (846) and SiC (317) [4]. Meanwhile, the heat and pressure resistance, radiation resistance, and unique UV transmittance make it widely applied in the fields of solar-blind UV photodetection, high-temperature, -frequency, -power microelectronic devices, gas-sensitive sensors, and photocatalysis [5,6]. Compared with GaN and SiC,  $\text{Ga}_2\text{O}_3$  not only has advantages in physical properties but also has superior conditions for growth techniques. Traditional growth methods, such as Czochralski method [7], floating zone method [8], and edge-defined film-fed growth method [9], are also applicable to  $\text{Ga}_2\text{O}_3$ , which creates

conditions for low-cost growth. Therefore,  $\text{Ga}_2\text{O}_3$  single crystal is a highly potential multifunctional ultrawide bandgap semiconductor material.

In accordance with different crystalline phases,  $\text{Ga}_2\text{O}_3$  has five polymorphs, labeled as  $\alpha$ ,  $\beta$ ,  $\gamma$ ,  $\delta$ , and  $\epsilon$ , among which,  $\beta$ - $\text{Ga}_2\text{O}_3$  has the most stable thermodynamic properties; thus,  $\beta$ - $\text{Ga}_2\text{O}_3$  is currently the most widely studied [10]. As with all semiconductor materials, monocrystalline  $\beta$ - $\text{Ga}_2\text{O}_3$  after growth will require a series of machining processes before application, in which wafer grinding is the most critical step to quickly remove material, improve packaging efficiency, and secure the physical strength and heat dissipation performance of the device. To ensure the wafer machining quality and reduce the following polishing time, the diamond wheel grinding based on the principle of wafer rotation is the most common method for wafer grinding [11,12]. However, the mechanical effects of grinding inevitably cause damage to the wafer subsurface, and some studies have shown that the damage inside the wafer can seriously affect the property and lifetime of the

device, which is to be avoided in the semiconductor field [13]. Few studies have been conducted on the machining damage of monocrystalline  $\beta\text{-Ga}_2\text{O}_3$ ; only Wu et al. [14–16] have done some work. They analyzed the damage pattern of monocrystalline  $\beta\text{-Ga}_2\text{O}_3$  through nanoindentation, micropillar compression, and nanogrinding tests and obtained the damage evolution at the micro–nano scale. That is, stacking faults and twins were first induced at low loads, then dislocations started to nucleate at relatively high loads. With the further increase in load, the lattice planes started to bend and finally cracks appeared. Although the above research demonstrated the damage evolution sequence of monocrystalline  $\beta\text{-Ga}_2\text{O}_3$ , this is significantly different from the grinding conditions and cannot represent the damage pattern under the grinding process. Therefore, targeted research should be performed on the subsurface damage caused by the grinding process of monocrystalline  $\beta\text{-Ga}_2\text{O}_3$ .

In this work, the surface morphology and subsurface damage of  $\beta\text{-Ga}_2\text{O}_3$  under rough, fine, and ultrafine grinding processes were observed by scanning electron microscopy (SEM), conventional and high-resolution transmission electron microscopy (TEM/HRTEM). The damage pattern under the processes was compared and analyzed on the basis of the grinding principle and material characteristics. The results in this work may provide guidance for the damage control of monocrystalline  $\beta\text{-Ga}_2\text{O}_3$  grinding process.

## 2 Experimental details

Commercial monocrystalline  $\beta\text{-Ga}_2\text{O}_3$  from Novel Crystal Technology (Japan) with a size of 10 mm × 10 mm × 1 mm was used as the sample. A (201)-oriented wafer was fabricated using the edge-defined film-fed growth method and handled by chemical mechanical polishing before grinding, and the surface roughness  $R_a$

was less than 1 nm. An ultraprecision grinder (VG401, MKII, Okamoto, Japan) based on the principle of wafer rotation was used. The grinder was equipped with air spindles, and the accuracy of feed rate was 1  $\mu\text{m}$ . The schematic and the equipment of the wafer rotation grinder are presented in Fig. 1. The resin bond diamond grinding wheels from Asahi Diamond Industrial (Japan) in grit sizes of SD600, SD5000, and SD12000 were selected for rough, fine, and ultrafine grinding. The grinding method was up grinding, and deionized water was used as a coolant. The grinding parameters are given in Table 1. Some of the parameters, such as the feed rate, differed to select the appropriate ones in accordance with the machining efficiency during the actual grinding process. After a series of preliminary grinding experiments, we chose the grinding parameters shown in the table.

After the grinding test, the morphology of samples was observed using a dual beam scanning electron microscope, and the cross section was observed using an FEI Tecnai F20 transmission electron microscope with the direction [010], as shown in the inset of Fig. 1(a). The TEM samples were prepared using FEI Scios focused ion beam, and a Pt film was deposited to protect the ground surface.

## 3 Results

### 3.1 Subsurface damage pattern in rough grinding

The subsurface damage pattern in rough grinding was extremely complicated. To characterize the damage type and analyze the damage pattern, the SEM image of the machined surface of sample 1 is shown in Fig. 2. Several areas were selected for TEM and HRTEM, as shown in Figs. 3 and 4.

Figures 2 and 3(a) demonstrate that the ground surface and cross-sectional morphology were extremely uneven.

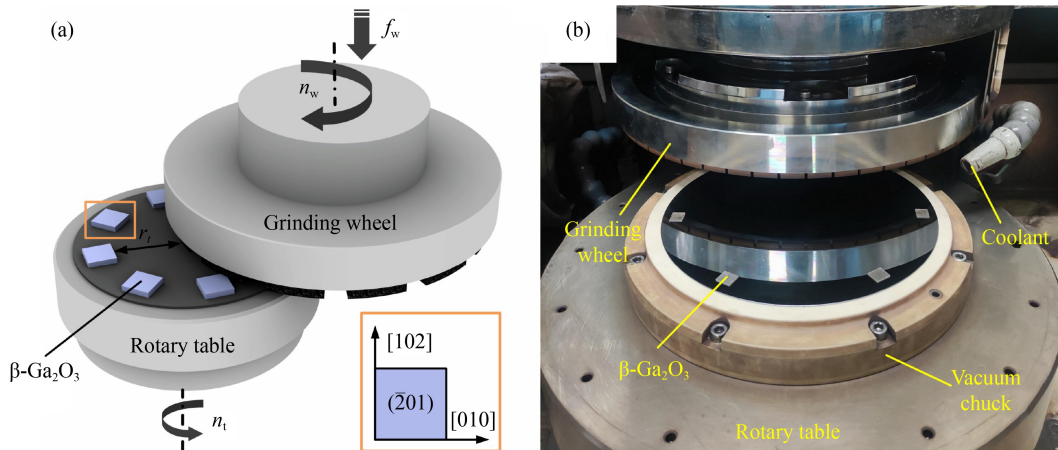


**Fig. 1** (a) Schematic of the wafer rotation grinder and (b) grinding equipment.

**Table 1** Experimental parameters in rough, fine, and ultrafine grinding processes

Sample	Wheel grit size	Wheel speed, $n_w/(r \cdot min^{-1})$	Table speed, $n_t/(r \cdot min^{-1})$	Feed rate, $f_w/(\mu m \cdot min^{-1})$	Grit radius, $R_g/\mu m$	Grit depth of cut, $d_g/nm$	Critical cutting depth, $d_c/nm$
1	SD600	2400	120	15	12.3	32.2	7.6
2	SD5000	2400	120	5	1.2	2.0	7.6
3	SD12000	2400	120	3	0.5	0.7	7.6

The SEM image illustrates that the ground surface was covered with broken pits and a typical brittle removal morphology. The depth of the damage layer was about 450 nm. The three regions of (b), (c), and (d) were chosen for HRTEM observation. In Fig. 3(b), the region did not have the characteristics of single crystal. However, numerous irregular grains with evident boundaries were seen. The corresponding selected area electron diffraction

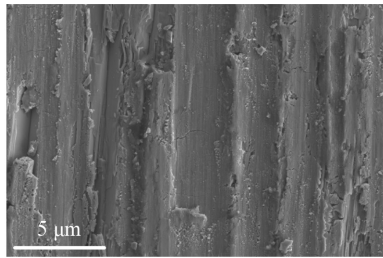


**Fig. 2** SEM image of the rough ground surface with the wheel grit size of SD600.

(SAED) pattern inserted in Fig. 3(b) proved that this region was mainly composed of nanocrystals with a thickness of 290 nm. In addition, nanovoids were seen clearly between nanocrystals. Some studies indicated that nanovoids are formed by the plastic flow of nanocrystals [17], and the mechanism for the generation of nanocrystals will be analyzed in the discussion. In Fig. 3(c), stacking faults existed along the (200)<sub>T</sub> lattice plane, which can be determined as a twinning zone in Fig. 3(d). The SAED pattern on the bottom right corner proved that the region below the twinning boundary had a normal stacking order with the twin boundary along the (201) lattice plane. Interlaced median cracks and transverse cracks were also found in Fig. 3(c), implying that the subsurface damage in the rough grinding process was serious [18].

As shown in Figs. 4(a) and 4(b), the thickness of the nanocrystalline layer is about 71.8 nm, which is quite different from that in Fig. 3(a), this indicated that the thickness of the nanocrystalline layer under rough

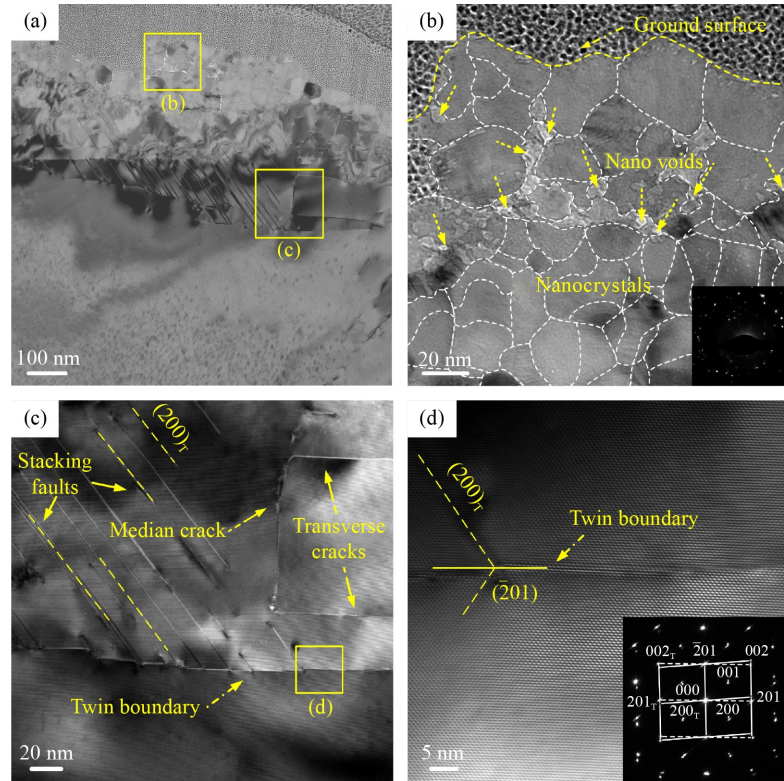


**Fig. 3** Bright-field cross-sectional TEM/HRTEM images of sample 1 (Part I): (a) overall morphology, (b) enlarged view at the top of the damage area, (c) enlarged view at the bottom of the damage area, and (d) enlarged view at the bottom of (c). The insets are the corresponding selected area electron diffraction patterns.

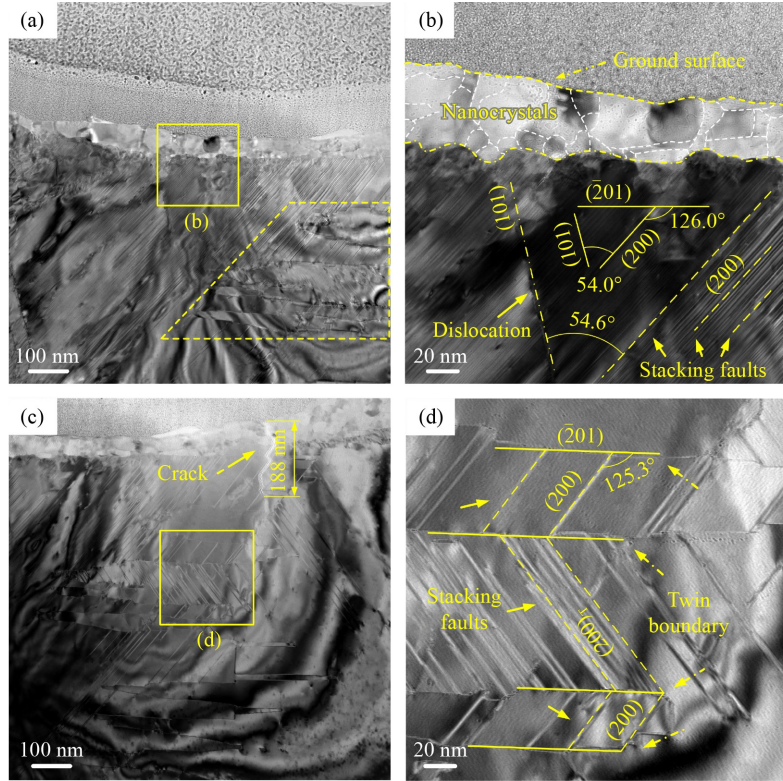


**Fig. 4** Bright-field cross-sectional TEM/HRTEM images of sample 1 (Part II): (a) partial morphology, (b) enlarged view at the top of (a), (c) another partial morphology, and (d) enlarged view in the middle of (c).

grinding condition was extremely uneven, and the formation mechanism of nanocrystals might be different. Dislocations along the (101) lattice plane and stacking faults along the (200) lattice plane were also found in Fig. 4(b). Their angle was about  $54.6^\circ$ , which was exactly close to the theoretical value of  $54.0^\circ$ . This result was consistent with the results obtained by Yamaguchi et al. [19]; the slip system in the monocrystalline  $\beta$ -Ga<sub>2</sub>O<sub>3</sub> comprised  $(\bar{2}01)$ ,  $(101)$ ,  $(\bar{3}01)$ , and  $(\bar{3}\bar{1}0)$ . Similarly, a crack with a depth of 188 nm was found in Fig. 4(c). It extended from the ground surface to the wafer interior, verifying the severity of subsurface damage under rough grinding conditions. In the dashed box in Fig. 4(a) and region (d) in Fig. 4(c), the damage patterns were multi-layer twin structures. Figure 4(d) illustrates that the twin boundaries were along the  $(\bar{2}01)$  lattice plane, and the stacking faults along the (200) lattice plane were distributed between the twin boundaries. The angle with the twin boundaries was  $125.3^\circ$ , which was close to the theoretical value of  $126.0^\circ$ , as indicated in Fig. 4(b) by solid lines. In the multilayer twin structures, the internal lattice arrangement was deflected for each layer of twin boundaries, specifically as stacking faults alternately along the (200) and  $(200)_T$  lattice planes. In subsurface damage research of monocrystalline  $\beta$ -Ga<sub>2</sub>O<sub>3</sub>, similar phenomena have not been found, and the formation mechanism is not yet clear.

### 3.2 Subsurface damage pattern in fine grinding

Figure 5 shows the surface morphology and Fig. 6 presents the subsurface damage of sample 2 in fine grinding. No obvious broken trace occurred on the surface, which indicated ductile removal. The subsurface damage depth was about 305 nm, which was significantly less than that in rough grinding. Hence, the wheel grit size exerted a greater influence on the subsurface damage depth. Three regions (b), (c), and (d) in Fig. 6(a) were selected for HRTEM observation. In Fig. 6(c), the SAED on the top right corner illustrates a nanocrystalline layer with a thickness of 38 nm, which was smaller than that in sample 1. Meanwhile, dislocations along the (101) lattice plane and high-density stacking faults along the (200) lattice plane were found in the lower part of the

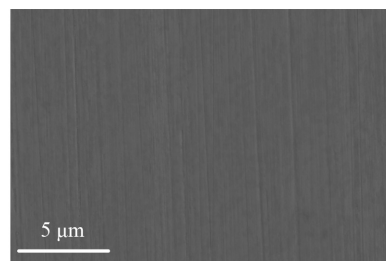


**Fig. 5** SEM image of the fine ground surface with the wheel grit size of SD5000.

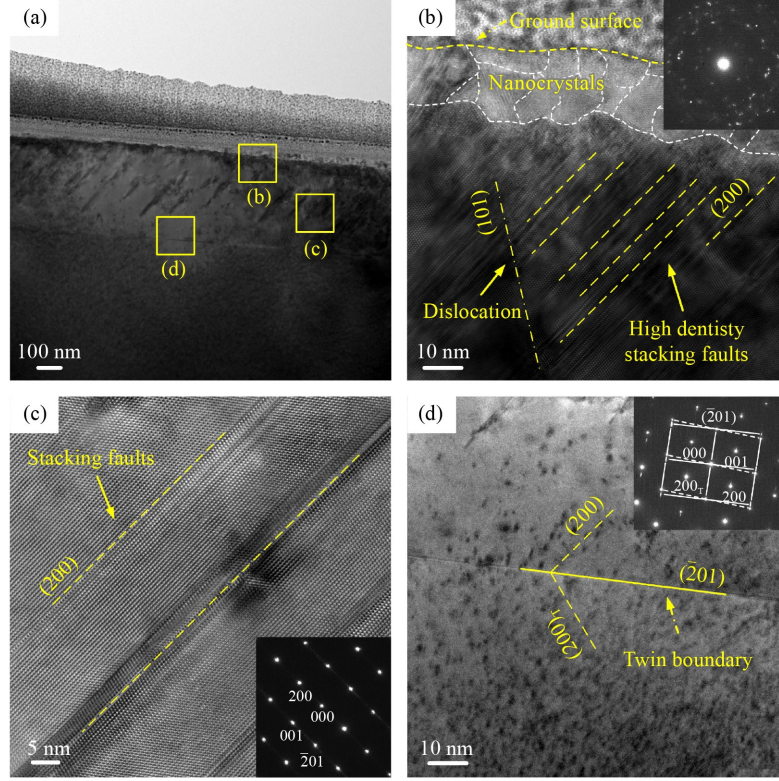


**Fig. 6** Bright-field cross-sectional TEM/HRTEM images of sample 2: (a) overall morphology, (b) enlarged view at the top of the damage area, (c) enlarged view in the middle of the damage area, and (d) enlarged view at the bottom of the damage area. The insets are the corresponding SAED patterns.

nanocrystalline layer, as demonstrated by the SAED in Fig. 6(c). The diffraction spot in the inset of Fig. 6(d) indicates the twins in this region with the twin boundary along the  $(\bar{2}01)$  lattice plane. To sum up, dislocations, stacking faults, and twins were also observed in fine grinding, which was basically consistent with rough grinding. The stacking faults and twins indicated that the stacking fault energy of monocrystalline  $\beta$ -Ga<sub>2</sub>O<sub>3</sub> is comparatively low [14], which is significantly different from the relatively high stacking fault energy of semiconductor materials, such as silicon [20,21] and gallium arsenide [22,23].

### 3.3 Subsurface damage pattern in ultrafine grinding

The SEM image shown in Fig. 7 reveals that the material was removed in the ductile region. The subsurface damage pattern in ultrafine grinding is illustrated in Fig. 8. Three regions (b), (c), and (d) were selected for HRTEM observation. Figure 8(b) illustrates that stacking faults existed along the (200) lattice plane in the damaged layer, which could be proved by the fast Fourier transform (FFT) on the bottom right corner. The SAED on the top right corner demonstrates that nanocrystals also existed in this region. Further analysis of the nanocrystalline layer, as shown in Fig. 8(c), revealed an amorphous layer with a thickness of 16.8 nm in the upper part of the

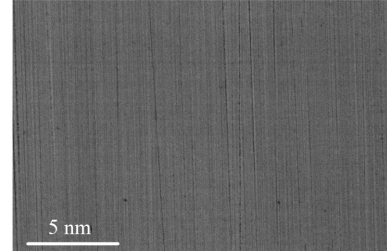


**Fig. 7** SEM image of the ultrafine ground surface with the wheel grit size of SD12000.

nanocrystalline layer, which had a clear boundary with the nanocrystalline layer. On the contrary, no amorphous phase was observed in rough and fine grinding, and the formation mechanism of the amorphous phase will be discussed later. Meanwhile, no twins were obtained in ultrafine grinding, indicating that the twins were not easily generated in this process. Figure 8(d) reveals that the stacking faults extended to 240 nm.

## 4 Discussion

From the research of the subsurface damage of monocrystalline  $\beta$ -Ga<sub>2</sub>O<sub>3</sub> in grinding process, the subsurface damage patterns in the three grinding samples present

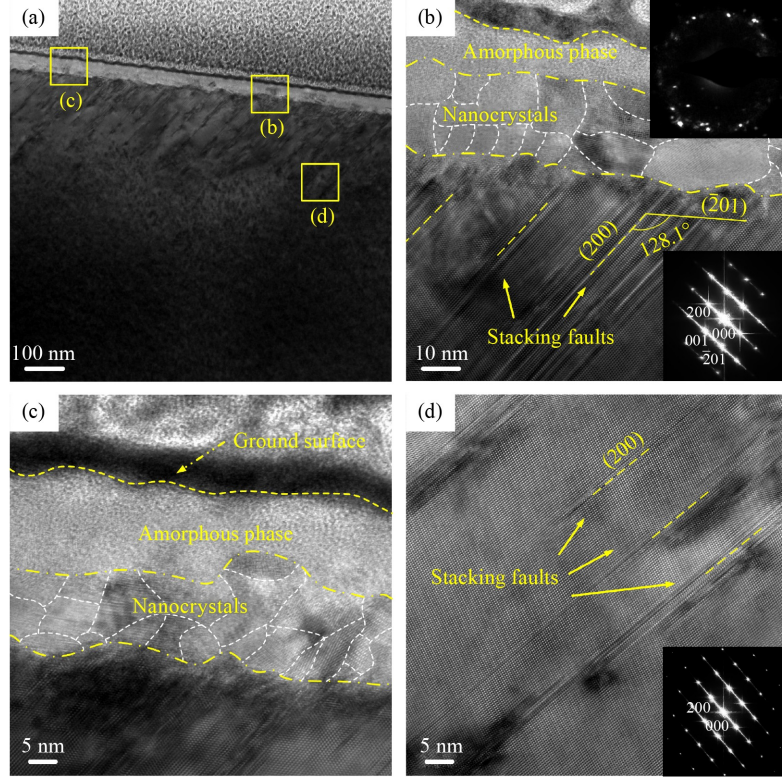


**Fig. 8** Bright-field cross-sectional TEM/HRTEM images of sample 3: (a) overall morphology, (b) enlarged view at the top of the damage area, (c) enlarged view on the top right corner of the damage area, and (d) enlarged view at the bottom of the damage area. The insets are the corresponding SAED and FFT patterns.

fewer difference. That is, nanocrystals, dislocations, high-density stacking faults, twins, and cracks are found in the rough grinding process; nanocrystals, dislocations, high-density stacking faults, and twins are observed in the fine grinding process; amorphous phase, nanocrystals, and stacking faults exist under the ultrafine grinding process. The schematic of subsurface damage patterns in the grinding processes is shown in Fig. 9. As the grit radius decreases, the grit depth of cut also decreases, the subsurface damage in rough grinding is complex, and the thickness of the damage layer is larger; meanwhile, the damage layer in fine and ultrafine grinding conditions gradually decreases. The formation mechanism of damage layer in different grinding conditions will be discussed below through the combination of grinding principle and material characteristics.

In wafer rotation grinding process, grit radius and grit depth of cut are often used to characterize the overall effect of grinding conditions, and they are critical to the contact relationship between grits and samples. The grit radius  $R_g$  and grit depth of cut  $d_g$  are calculated using Eqs. (1) [24] and (2) [25], and the detailed values are shown in Table 1.

$$R_g = \frac{14}{M^{1.1}}, \quad (1)$$

where  $M$  is the wheel mesh size.

$$d_g = 3.71 R_g \left( \frac{f_w r_t n_t}{L_w W_w V_g n_w^2} \right)^{0.4}, \quad (2)$$

the detailed values of  $f_w$ ,  $n_t$ , and  $n_w$  are shown in Table 1.  $r_t$  is the distance from the table center to the sample, and its value is 35 mm in this study. The width of the wheel segment  $W_w$  is 3.0 mm, the length of the wheel circumference  $L_w$  is 1100.0 mm, and the grit volume ratio of the wheel segment  $V_g$  is 0.25.

An amended model for estimating critical cutting depth ( $d_c$ ) can be used to evaluate the ductile grinding process in monocrystalline  $\beta$ -Ga<sub>2</sub>O<sub>3</sub>, as shown follows [26]:

$$d_c = 8.7 \left( \frac{H}{E} \right)^{1/2} \left( \frac{K_c}{H} \right)^2, \quad (3)$$

where the hardness ( $H$ ) and elastic modulus ( $E$ ) are 14.5 and 195.7 GPa, respectively [27], and the fracture toughness ( $K_c$ ) is 0.82 MPa·m<sup>1/2</sup> [28]. After calculation, we obtain the  $d_c$  of monocrystalline  $\beta$ -Ga<sub>2</sub>O<sub>3</sub> as 7.6 nm, and the value is shown in Table 1.

The subsurface damage thickness, grit radius, and grit depth of cut are illustrated in Fig. 10. It is obviously demonstrated that the total damage thickness and the nanocrystalline thickness gradually decrease with the rough, fine, and ultrafine grinding processes, as shown in Fig. 10(a). The minimum damage thickness is obtained in

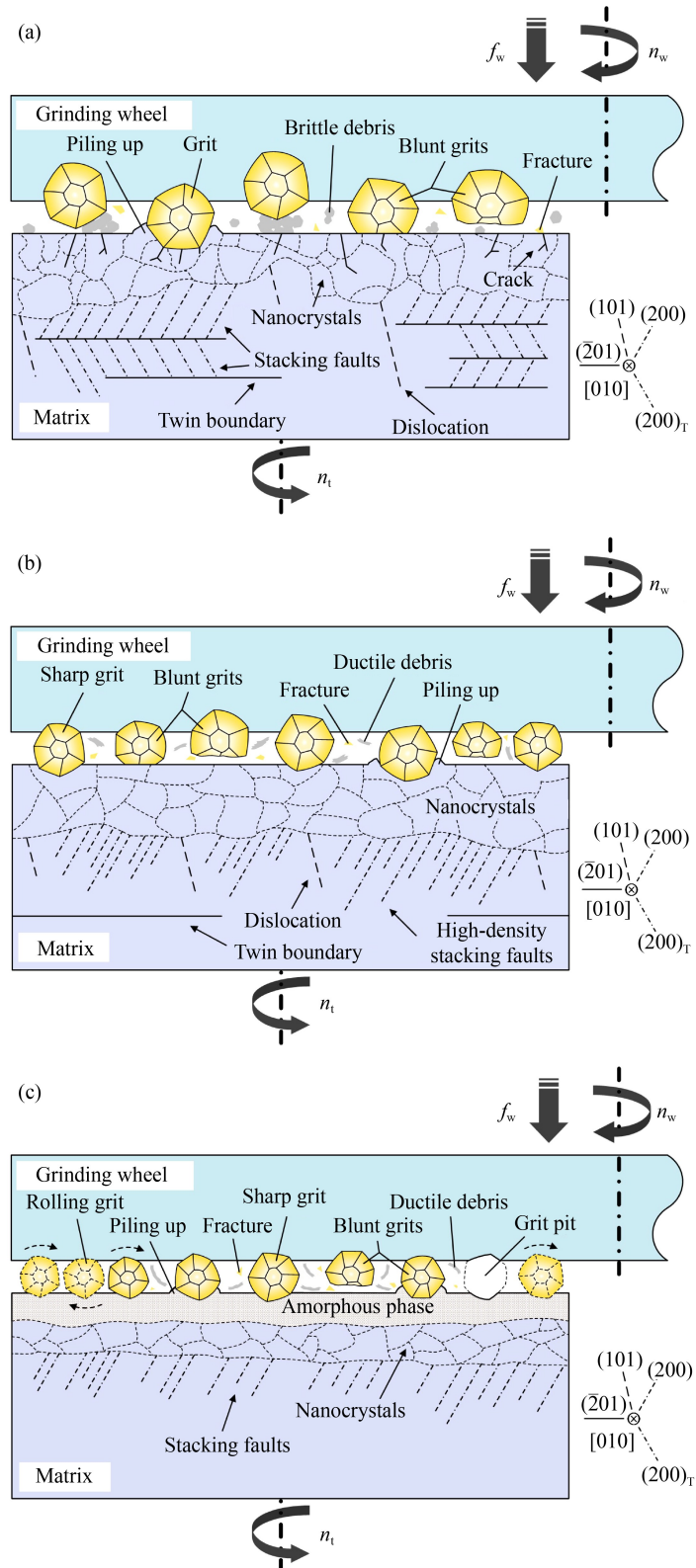


**Fig. 9** Schematic of subsurface damage patterns in grinding processes: (a) rough grinding process, (b) fine grinding process, and (c) ultrafine grinding process.

ultrafine grinding process with a value of 240 nm. In addition, combined with the calculated critical cutting depth, SD600 is brittle grinding, whereas SD5000 and

SD12000 are ductile grinding, as shown in Fig. 10(b). This result is consistent with the results we obtained from Figs. 2, 5, and 7.

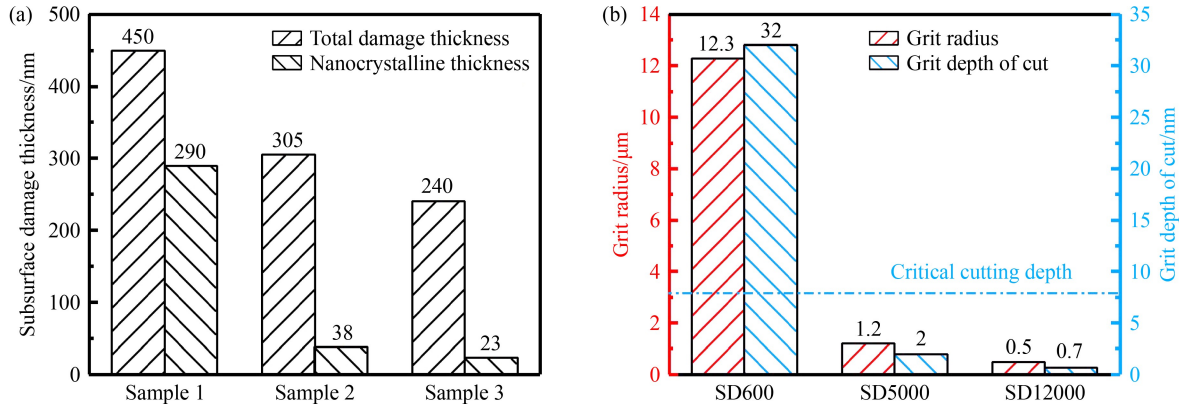


**Fig. 10** (a) Subsurface damage thickness of samples and (b) grit radius and grit depth of cut of grinding wheels.

#### 4.1 Formation mechanism of subsurface damage in rough grinding

For rough grinding, the grit radius of the SD600 wheel is relatively large, with a size of about  $12.3 \mu\text{m}$ , and the grit depth of cut is about  $32 \text{ nm}$ . The frictional extrusion between grits and samples during the grinding process is intense, the strain rate is high, and the contact stress of the blunt grits is relatively large [29]; the value can reach the critical point of monocrystal to nanocrystal. Another point that cannot be ignored is the auxiliary extrusion effect of the grinding debris. From the above analysis, the material removed in rough grinding presents brittle grinding. During the process, substantial brittle and broken large-sized debris are generated [30]. Most of the debris are taken away by the coolant, but some of the residual debris are dragged by the rotation of the grinding wheel and forced into the grinding process. This process results in a dynamic extrusion system of grits–brittle debris–samples, which basically does not have cutting ability. Moreover, a nanocrystalline layer with uneven thickness is generated, as shown in Figs. 3(b) and 4(b). Meanwhile, cracks exist in the surface layer of sample 1, which are due to the high strain rate during the rough grinding process. The intense mechanical effects cause the internal stress in the subsurface layer of the material to exceed the fracture limit, resulting in cracks, as shown in Figs. 3(c) and 4(c). Dislocations, high-density stacking faults, and twins are also found in sample 1. The occurrence of stacking faults and twins is related to the material characteristics. The schematic of subsurface damage patterns in rough grinding is shown in Fig. 9(a).

#### 4.2 Formation mechanism of subsurface damage in fine grinding

According to the damage pattern of fine grinding, the grit size of the SD5000 wheel is between those of SD600 and SD12000 wheels; it is about  $1.2 \mu\text{m}$ , and the grit cutting depth is  $2 \text{ nm}$ . Ductile grinding is carried out between the grits and the samples, in which the ductile debris has a

minimal effect on the grinding process [31,32]. With the grinding process, blunt grits begin to generate an extrusion effect with the samples, and their contact stress reaches the critical point for nanocrystals. However, due to the limitation of the grit radius, the contact stress is less than that of the SD600 grinding wheel. Therefore, the nanocrystalline thickness in sample 2 is thinner than that in sample 1. Similarly, dislocations, stacking faults, and twins exist in sample 2. No cracks are found because the material removal method in fine grinding is ductile removal and the mechanical effects are less than those of rough grinding. The schematic of subsurface damage patterns in fine grinding is shown in Fig. 9(b).

#### 4.3 Formation mechanism of subsurface damage in ultrafine grinding

As to sample 3, SD12000 is an ultrafine grinding wheel with a grit radius of  $0.5 \mu\text{m}$  and a cut depth of  $0.7 \text{ nm}$ . The material removal mechanism is completely ductile grinding. The ultrafine debris has almost no effect on the grinding process. To realize continuous grinding ability, the self-sharpening process of ultrafine grinding wheels is generally required to be high [33,34], but the grits in the grinding wheels are likely to fall off from the base. Then, the movement of grits becomes three-body wear [35,36] and starts to scratch irregularly with the samples in a large amount. Meanwhile, the grits of ultrafine grinding wheels are small in size and likely to be blunt. Consequently, the grinding process of ultrafine grinding wheels is often accompanied by large grinding force, specific grinding energy, and heat, which induces the generation of an amorphous phase. In this study, the amorphous layer is found only in ultrafine grinding. Gao et al. [16] suggested that the generation of  $\beta\text{-Ga}_2\text{O}_3$  amorphous layer might be related to the heat generated during grinding and the specific grinding energy. More energy is required for the generation of an amorphous phase than that for a nanocrystals, which is basically consistent with the conclusion obtained in this study. Also, stacking faults remain. The schematic of subsurface

damage patterns in ultrafine grinding is shown in Fig. 9(c).

The intense plastic deformation under high strain rate conditions will refine the grain size to the nanoscale, which leads to dislocation annihilation, recombination, rearrangement to form cells, and subgrain structures with nanoscale dimensions; however, this process is also affected by many variables, such as plastic deformation conditions and material characteristics [37]. The grinding process has a very high strain rate, and the mechanical interaction between grits and samples will cause complicated and severe plastic deformation of the surface and subsurface material. Previous investigations have demonstrated that the cutting points on grits are mostly negative rake angle ( $\gamma_g$ ). The value of  $\gamma_g$  is from  $-15^\circ$  to  $-60^\circ$  [24]. With the grinding process, the grits will be blunted easily, and the negative rake will further increase. The large negative rake will lead to a large cutting force and a high strain rate during the grinding. The cutting process is dominated by extrusion. At this moment, numerous defects will be formed in the plastic deformation zone under the complicated stress status [18,38].

In addition, monocrystalline  $\beta$ -Ga<sub>2</sub>O<sub>3</sub> has low stacking fault energy. Dislocations are easily decomposed into partial dislocations and generate stacking faults during the plastic deformation process. Extended dislocations have a large width, causing a difficulty for cross slip. Local stress concentration occurs easily during the grinding process, thereby inducing deformation twins. The formation mechanism of nanocrystals becomes the co-coordination of dislocation slip, intercross, and twinning [39–41]. Subsequently, the complicated stress status will result in the rotation of a tiny crystalline body (at nanoscale), eventually forming nanocrystals with different orientations. Therefore, for the monocrystalline  $\beta$ -Ga<sub>2</sub>O<sub>3</sub> with low stacking fault energy, the grinding process with high strain rate is likely to induce nanocrystals [16]. Figures 3(b), 4(b), 6(b), and 8(c) prove this view.

As shown in Fig. 10(b), the grit depth of cut in large grits is larger. Consequently, the blunting phenomenon of grits is obvious, the negative rake of cutting points is large, and the extrusion depth of blunted grits is also large. Then, due to the auxiliary extrusion of large-sized brittle debris, the thickness of the nanocrystalline layer is large and uneven under the rough grinding process. As the grit radius and grit depth of cut decrease, the material is removed by ductile regime [42]; at this time, the interaction depth of the blunted grits decreases, and the thickness of the nanocrystalline layer is also decreased, as shown in Fig. 10(b). The grit radius and grit depth of cut of the ultrafine grinding wheel are much smaller than those of rough and fine grinding wheels. Owing to the extremely small depth of cut and the limitation of the self-sharpening of the grinding wheel, the thickness of the nanocrystalline layer induced by the SD12000 ultrafine

grinding wheel is minimal, and an amorphous phase is also generated.

In summary, the grinding conditions and material characteristics may be the key factors affecting the transformation of monocrystalline  $\beta$ -Ga<sub>2</sub>O<sub>3</sub> to nanocrystals and amorphous phase. Nevertheless, the critical condition requires further research. Given the low stacking fault energy of monocrystalline  $\beta$ -Ga<sub>2</sub>O<sub>3</sub>, stacking faults and twins are easy to occur during the grinding process. Even under the ultrafine grinding conditions, stacking faults still exist.

## 5 Conclusions

In the research of subsurface damage pattern and formation mechanism of monocrystalline  $\beta$ -Ga<sub>2</sub>O<sub>3</sub> in grinding process, damage models under different grinding processes were established on the basis of the grinding principle, and the mechanism of the grit mechanical effect on the subsurface damage pattern was revealed. The damage pattern in rough grinding was relatively serious and complicated. Specific manifestations were nanocrystals, dislocations along the (101) lattice plane, stacking faults along the (200) and (200)<sub>T</sub> lattice planes, a twin boundary along the (201) lattice plane, and cracks. Meanwhile, nanocrystals, stacking faults along the (200) lattice plane, dislocations along the (101) lattice plane, and a twin boundary along the (201) lattice plane were observed in the fine grinding process. Amorphous phase, nanocrystals, and stacking faults along the (200) lattice plane existed in the ultrafine grinding process. The damage patterns of the grinding processes were minimally different. The subsurface damage thickness decreased with the reduction in the grit radius and the grit depth of cut. Nanocrystalline layers were found in the rough, fine, and ultrafine grinding processes, but an amorphous phase was observed only in ultrafine grinding. The formation mechanism of nanocrystals and amorphous phase was related to the grinding conditions and material characteristics.

**Acknowledgements** This research was financially supported by the National Natural Science Foundation of China (Grant Nos. 51975091, 51991372, and 51735004), the National Key R&D Program of China (Grant No. 2018YFB1201804-1), the Lab of Space Optoelectronic Measurement & Perception (LabSOMP-2019-05), and Jiangsu Key Laboratory of Precision and Micro-Manufacturing Technology.

## References

1. Pearton S J, Yang J C, Cary P H IV, Ren F, Kim J, Tadjer M J, Mastro M A. A review of Ga<sub>2</sub>O<sub>3</sub> materials, processing, and devices. *Applied Physics Reviews*, 2018, 5(1): 011301
2. Gao S, Li H G, Kang R K, He Y W, Zhu X L. Recent advance in

- preparation and ultra-precision machining of new generation semiconductor material of  $\beta$ -Ga<sub>2</sub>O<sub>3</sub> single crystals. *Journal of Mechanical Engineering*, 2021, 57(9): 213–232 (in Chinese)
3. Higashiwaki M.  $\beta$ -gallium oxide devices: progress and outlook. *Physica Status Solidi*, 2021, 15(11): 2100357
  4. Kaur D, Kumar M. A strategic review on gallium oxide based deep-ultraviolet photodetectors: recent progress and future prospects. *Advanced Optical Materials*, 2021, 9(9): 2002160
  5. Zhou H, Zhang J C, Zhang C F, Feng Q, Zhao S L, Ma P J, Hao Y. A review of the most recent progresses of state-of-art gallium oxide power devices. *Journal of Semiconductors*, 2019, 40(1): 011803
  6. Tse G. The electronic, optical, elastic, and mechanical properties of triclinic Ga<sub>2</sub>O<sub>3</sub> with density functional theory. *Computational Condensed Matter*, 2021, 29: e00593
  7. Galazka Z, Irmscher K, Uecker R, Bertram R, Pietsch M, Kwasniewski A, Naumann M, Schulz T, Schewski R, Klimm D, Bickermann M. On the bulk  $\beta$ -Ga<sub>2</sub>O<sub>3</sub> single crystals grown by the Czochralski method. *Journal of Crystal Growth*, 2014, 404: 184–191
  8. Arima-Osonoi H, Yamazaki K, Simura R, Sugawara T, Yubuta K, Sugiyama K, Yoshiasa A. Local structure investigations of Sn and Mn doped in  $\beta$ -Ga<sub>2</sub>O<sub>3</sub> by X-ray absorption spectroscopy. *Journal of Crystal Growth*, 2021, 570: 126223
  9. Nikolaev V I, Maslov V, Stepanov S I, Pechnikov A I, Krymov V, Nikitina I P, Guzilova L I, Bougrov V E, Romanov A E. Growth and characterization of  $\beta$ -Ga<sub>2</sub>O<sub>3</sub> crystals. *Journal of Crystal Growth*, 2017, 457: 132–136
  10. Zhang N J, Liu H Y, Sai Q L, Shao C Y, Xia C T, Wan L Y, Feng Z C, Mohamed H F. Structural and electronic characteristics of Fe-doped  $\beta$ -Ga<sub>2</sub>O<sub>3</sub> single crystals and the annealing effects. *Journal of Materials Science*, 2021, 56(23): 13178–13189
  11. Gao S, Kang R K, Dong Z G, Zhang B. Edge chipping of silicon wafers in diamond grinding. *International Journal of Machine Tools and Manufacture*, 2013, 64: 31–37
  12. Dong Z G, Zhang Q, Liu H J, Kang R K, Gao S. Effects of taping on grinding quality of silicon wafers in backgrinding. *Frontiers of Mechanical Engineering*, 2021, 16(3): 559–569
  13. Zhang X D, Yang C L, Zhang Y M, Hu A M, Li M, Gao L M, Ling H Q, Hang T. Sub-surface damage of ultra-thin monocrystalline silicon wafer induced by dry polishing. *Electronic Materials Letters*, 2020, 16(4): 355–362
  14. Wu Y Q, Gao S, Huang H. The deformation pattern of single crystal  $\beta$ -Ga<sub>2</sub>O<sub>3</sub> under nanoindentation. *Materials Science in Semiconductor Processing*, 2017, 71: 321–325
  15. Wu Y Q, Gao S, Kang R K, Huang H. Deformation patterns and fracture stress of beta-phase gallium oxide single crystal obtained using compression of micro-pillars. *Journal of Materials Science*, 2019, 54(3): 1958–1966
  16. Gao S, Wu Y Q, Kang R K, Huang H. Nanogrinding induced surface and deformation mechanism of single crystal  $\beta$ -Ga<sub>2</sub>O<sub>3</sub>. *Materials Science in Semiconductor Processing*, 2018, 79: 165–170
  17. Li C, Zhang F H, Wu Y Q, Zhang X. Influence of strain rate effect on material removal and deformation mechanism based on ductile nanoscratch tests of Lu<sub>2</sub>O<sub>3</sub> single crystal. *Ceramics International*, 2018, 44(17): 21486–21498
  18. Zhang Z Y, Wu Y Q, Huang H. New deformation mechanism of soft-brittle CdZnTe single crystals under nanogrinding. *Scripta Materialia*, 2010, 63(6): 621–624
  19. Yamaguchi H, Kuramata A, Masui T. Slip system analysis and X-ray topographic study on  $\beta$ -Ga<sub>2</sub>O<sub>3</sub>. *Superlattices and Microstructures*, 2016, 99: 99–103
  20. Föll H, Carter C B. Direct TEM determination of intrinsic and extrinsic stacking fault energies of silicon. *Philosophical Magazine A*, 1979, 40(4): 497–510
  21. Aerts E, Delavignette P, Siems R, Amelinckx S. Stacking fault energy in silicon. *Journal of Applied Physics*, 1962, 33(10): 3078–3080
  22. Gerthsen D, Carter C B. Stacking-fault energies of GaAs. *Physica Status Solidi (a)*, 1993, 136(1): 29–43
  23. Li Z C, Liu L, Wu X, He L L, Xu Y B. TEM observation of the phase transition in indented GaAs. *Materials Letters*, 2002, 55(3): 200–204
  24. Malkin S, Guo C. *Grinding Technology: Theory and Applications of Machining With Abrasives*. New York: Industrial Press, 2008
  25. Young H T, Liao H T, Huang H Y. Novel method to investigate the critical depth of cut of ground silicon wafer. *Journal of Materials Processing Technology*, 2007, 182(1–3): 157–162
  26. Huang H, Lawn B R, Cook R F, Marshall D B. Critique of materials-based models of ductile machining in brittle solids. *Journal of the American Ceramic Society*, 2020, 103(11): 6096–6100
  27. Wang Y Q, Li X L, Wu Y Q, Mu D K, Huang H. The removal mechanism and force modelling of gallium oxide single crystal in single grit grinding and nanoscratching. *International Journal of Mechanical Sciences*, 2021, 204: 10656
  28. He Y W. Surface damage formation mechanism of ultra-precision grinding of monocrystalline gallium oxide. Thesis for the Master's Degree. Dalian: Dalian University of Technology, 2021 (in Chinese)
  29. Wang Y, Zou J, Huang H, Zhou L, Wang B L, Wu Y Q. Formation mechanism of nanocrystalline high-pressure phases in silicon during nanogrinding. *Nanotechnology*, 2007, 18(46): 465705
  30. Yang Y P, Ji Y M. Experimental study on grinding damage control of optical materials. *Diamond & Abrasives Engineering*, 2020, 40(2): 84–88 (in Chinese)
  31. Bifano T G, Dow T A, Scattergood R O. Ductile-regime grinding: a new technology for machining brittle materials. *Journal of Engineering for Industry*, 1991, 113(2): 184–189
  32. Huang H, Li X L, Mu D K, Lawn B R. Science and art of ductile grinding of brittle solids. *International Journal of Machine Tools and Manufacture*, 2021, 161: 103675
  33. Zhou Z Z, Feng K P, Lv B H, Fan H W, Yuan J L. Analysis on wear of self-sharpening fine super-hard abrasive tool. *Advanced Materials Research*, 2013, 797: 528–533
  34. Fujimoto M, Ichida Y, Sato R. Wear characteristics of vitrified cBN grinding wheels. *Journal of Advanced Mechanical Design, Systems, and Manufacturing*, 2008, 2(4): 570–578
  35. Dwyer-Joyce R S, Sayles R S, Ioannides E. An investigation into the mechanisms of closed three-body abrasive wear. *Wear*, 1994, 175(1–2): 133–142

36. Evans C J, Paul E, Dornfeld D, Lucca D A, Byrne G, Tricard M, Klocke F, Dambron O, Mullany B A. Material removal mechanisms in lapping and polishing. *CIRP Annals*, 2003, 52(2): 611–633
37. Koch C C, Ovid'ko I A, Seal S, Veprek S. *Structural Nanocrystalline Materials: Fundamentals and Applications*. Cambridge: Cambridge University Press, 2007
38. Li C, Piao Y C, Meng B B, Hu Y X, Li L Q, Zhang F H. Phase transition and plastic deformation mechanisms induced by self-rotating grinding of GaN single crystals. *International Journal of Machine Tools and Manufacture*, 2022, 172: 103827
39. Balogh L, Ungár T, Zhao Y H, Zhu Y T, Horita Z, Xu C, Langdon T G. Influence of stacking-fault energy on microstructural characteristics of ultrafine-grain copper and copper-zinc alloys. *Acta Materialia*, 2008, 56(4): 809–820
40. Zhang Z Y, Xu C G, Zhang X Z, Guo D M. Mechanical characteristics of nanocrystalline layers containing nanotwins induced by nanogrinding of soft-brittle CdZnTe single crystals. *Scripta Materialia*, 2012, 67(4): 392–395
41. Randle V. Mechanism of twinning-induced grain boundary engineering in low stacking-fault energy materials. *Acta Materialia*, 1999, 47(15–16): 4187–4196
42. Zhang L C, Zarudi I. Towards a deeper understanding of plastic deformation in mono-crystalline silicon. *International Journal of Mechanical Sciences*, 2001, 43(9): 1985–1996